

## A JOINT SUNYAEV-ZEL'DOVICH EFFECT AND X-RAY ANALYSIS OF ABELL 3667

C.M. CANTALUPO<sup>1</sup>, A.K. ROMER, J.B. PETERSON, P. GOMEZ, G. GRIFFIN, M. NEWCOMB, R.C. NICHOL

Department of Physics, Carnegie Mellon University, 5000. Forbes Ave., Pittsburgh, PA-15213

December 18th 2002

## ABSTRACT

We present a 40GHz (7.5 mm) raster scan image of a  $3.6^\circ \times 2^\circ$  region centered on the low redshift ( $z = 0.055$ ) cluster of galaxies Abell 3667. The cluster was observed during the Antarctic winter of 1999 using the Corona instrument (15.7' FWHM beam) on the Viper Telescope at the South Pole. The Corona image of A3667 is one of the first direct (*i.e.* rather than interferometer) thermal Sunyaev-Zel'dovich effect images of a low redshift cluster. The brightness temperature decrement at the X-ray centroid ( $20^h 12^m 28.9^s, -56^\circ 49' 51''$  J2000) was measured to be  $\Delta T_{\text{CMB}} = -154 \mu\text{K}$ . We have used the 40GHz map of A3667 in conjunction with a deep ROSAT PSPC (X-ray) image of the cluster, to make a measurement of the Hubble Constant. We find  $H_0 = 64_{-30}^{+96} \text{ km s}^{-1} \text{ Mpc}^{-1}$  (68% confidence interval). Our  $H_0$  calculation assumes that the cluster can be described using an isothermal, tri-axial ellipsoidal,  $\beta$ -model and includes several new analysis techniques including an automated method to remove point sources from X-ray images with variable point spread functions, and an efficient method for determining the errors in multi-parameter maximum likelihood analyzes. The large errors on the  $H_0$  measurement are primarily due to the statistical noise in the Corona image. We plan to increase the precision of our measurement by including additional clusters in our analysis and by increasing the sensitivity of the Viper SZE maps.

## 1. INTRODUCTION

The Sunyaev-Zel'dovich effect (Sunyaev & Zel'dovich 1972, SZE hereafter) describes the inverse Compton scattering of cosmic microwave background (CMB) photons by energetic free electrons. For instance, the random thermal motions of electrons trapped in the potential wells of clusters of galaxies result in a frequency dependent change in CMB intensity known as the thermal SZE. Similarly, the bulk peculiar motion of these electrons results in frequency independent change known as the kinetic SZE. Observations of the thermal and kinetic SZE using either single dish telescopes (*e.g.* Mason, Myers & Readhead 2001; Pointecouteau et al. 2001 & 2002; De Petris et al. 2002) or interferometric techniques (*e.g.* Jones et al. 2001; Reese et al. 2001 & 2002; Udomprasert, Mason & Readhead 2001) have improved dramatically in recent years (see Birkinshaw 1999 for a recent review). Measurements of the SZE have been used for a variety of scientific applications, including the estimation of the Hubble Constant (*e.g.* Mason, Myers, & Readhead 2001; Jones et al. 2001; Reese et al. 2002); determinations of the fraction, by mass, of baryons in the Universe (*e.g.* Grego et al. 2001); X-ray independent measurements of cluster temperatures (*e.g.* Pointecouteau et al. 2002); and constraints on cluster peculiar velocities (Holzapfel et al. 1997b, LaRoque et al. 2002).

The technique of interferometric SZE imaging is now well established. By contrast, only recently has it become possible to generate direct (rather than aperture synthesis) SZE images using single dish telescopes. To date, only two clusters, RX J1347-1145 & RX J2228+2037, both at  $z \simeq 0.4$ , have published direct SZE images (Pointecouteau et al. 1999, 2001 & 2002; Komatsu et al. 2001). We

report here a third direct SZE image. This 40 GHz (7.5 mm) image of the ( $z = 0.055$ , Sodre et al. 1992) Abell cluster (Abell, Corwin, & Olowin 1989) A3667 was made using the Viper telescope at the South Pole as part of the Viper Sunyaev-Zel'dovich Survey (VSZS). The VSZS aims to study a complete sample of southern clusters at radio/microwave, optical and X-ray wavelengths and its goals include the measurement of the Hubble Constant. We chose to study A3667 as our initial VSZS target because, as one of the brightest X-ray ( $L_{0.5-2.0\text{keV}} = 4.1 \times 10^{44} \text{ ergs s}^{-1}$ , David et al. 1999) clusters in the REFLEX catalog (Böhringer et al. 2001), A3667 is expected to have a strong SZE signal. A3667 is also one of the best studied clusters in the sky. Supporting data at other wavelengths include: X-ray imaging and spectroscopy (ROSAT: Knopp, Henry & Briel 1996; ASCA: Markevitch, Sarazin, Vikhlinin 1999; White et al. 2000; BeppoSAX: Fusco-Femiano et al. 2001; Chandra: Vikhlinin, Markevitch & Murray 2001 a& b; XMM), optical data in the form of images, weak lensing mass maps and multi-object spectroscopy (*e.g.* Joffre et al. 2000; Katgert et al. 1998), and radio maps (Röttgering et al. 1997; Hunstead et al. 1999). In addition, A3667 has been the focus of three-dimensional MDH/N-body numerical simulations (Roettiger, Burns & Stone 1999).

An outline of the paper is as follows. In section 2 we review our observing strategy and data reduction methods. We also present the Corona map of the area around A3667. In section 3 we describe a joint fit, to an isothermal, tri-axial ellipsoidal  $\beta$ -model, to the ROSAT Position Sensitive Proportional Counter (PSPC) and Corona images of A3667 and present an estimate of the Hubble Constant. In section 4, we present conclusions and discuss future plans for cluster observations with Viper.

<sup>1</sup>Current affiliation: University of California Berkeley Space Sciences Laboratory

## 2. THE CORONA OBSERVATION OF A3667

The observations presented herein were made with the 2.15 meter Viper telescope during the austral winter of 1999. At the time, Viper was fitted with a two pixel receiver instrument known as Corona that measured the total incident power in the frequency range 38 to 44 GHz ( $\bar{\nu} = 40$ , Coble et al. 1999) using HEMT (high electron mobility transistor) amplifiers. The following features make Viper ideally suited to the observation of low redshift clusters such as A3667; its location at the South Pole, the two story conical shield and the flat chopping tertiary mirror that sweeps the telescope beam backward and forward by up to  $3.6^\circ$  in co-elevation. The South Pole is one of the driest sites in the world (Peterson et al. 2002), the shield minimizes ground pick up and the chopper permits observations of clusters that are extended over large areas of the sky.

Using Corona on Viper, we have generated a 40 GHz image of a  $2^\circ \times 3.6^\circ$  region centered on A3667. We did so using a raster scan technique that involved taking measurements during eight complete chopper cycles at each of 25 fixed elevation positions separated by  $300''$  (roughly one third of a beam). For the A3667 observation, we used a  $3.6^\circ$  chopper throw (the maximum possible) and read out the instrument 512 times per  $2.15 \text{ s}^{-1}$  chopper cycle, resulting in measurements separated by  $50.6''$  in the azimuth direction. Including overheads, each raster scan map took a little over a minute to complete. In total, 3,103 raster scans were made over six contiguous days: May 28, 29, 30, 31 & June 1, 2 1999. Every two hours during that period, the Carina nebula was observed as a pointing check. During our observation, the Corona beam pattern was well described by a radially symmetric Gaussian with a FWHM of  $0.261^\circ$  ( $15.7'$ ) and the total calibration uncertainty was 8% (Peterson et al 2000).

The raster scan data were initially stored as a time stream of detector voltages. The first stage of the analysis was to apply a filter to the time stream. This corrected for the detector response function; removed high frequency noise; and eliminated any signal coupled to the power mains, by removing harmonics of 60 Hz. Next noisy and/or poor quality scans were flagged and cut from the analysis: Those with any  $\geq 5\sigma$  voltage spikes, those with tracking or chopping position errors greater than two arcminutes, those for which the amplifiers were warmer than 25K, those with excessive noise at harmonics of 60 Hz, those with rapidly varying voltages and those with an unusually high average voltage. We note that the first data cut removed electrical interference in the data, and the latter two helped remove time periods when clouds were moving across the field of view. Once all seven cuts had been applied, 1518 scans of the initial 3103 remained or  $\simeq 36$  hours of integration.

As it is conventional to express CMB intensity changes as changes in brightness temperature,  $\Delta T$ , the next stage of the analysis involved converting the voltage time stream into a  $\Delta T$  time stream using the detector calibration. Then the 1518 sets of time stream were converted into grid maps consisting of 512 rows and 25 columns each. Next, the grid maps needed to be corrected for contaminating signals known collectively as ‘‘chopper synchronous offsets’’. These offsets can include signals originating from

the ground, the atmosphere and the telescope components. The offset level varies with chopper position because, as the chopper moves, the focal plane is illuminated by different areas of the telescope optics (see Peterson et al. 2000). Under the assumption that the offsets change linearly with elevation, and maintained the same general waveform in the azimuth (chopping) direction, the offsets were removed from the inner regions of the scans as follows. The linear component in the elevation direction was removed by fitting to the top and bottom 4 rows in each of the columns. Next, the linear component in the azimuth direction was removed by fitting to the first and last 50 columns in each of the rows. After offset correction, the  $512 \times 25$  points in the offset subtracted grid maps were assigned sky coordinates using the Peterson et al. (2000) telescope pointing model. Finally, the maps were converted into fully sampled images with  $113'' \times 113''$  pixels. Linear interpolation in the elevation direction was used to create these images because the grid points in the raster scan were separated by  $300''$  in elevation (compared to  $51''$  in azimuth).

In Figures B1 and B2 we present the result of averaging the 1,518 fully sampled images together. In these Figures, the data have been smoothed with a  $10.3'$  FWHM Gaussian kernel, which gives them an effective resolution of  $18'$  FWHM (the beam size of the instrument was  $15.7'$ ). The effective beam FWHM has been represented by the red circle in the bottom right corner of Figure B2. In Figure B1 we present the full dimensions of the co-added image, including the edge regions used for the offset subtraction. The elongated blue (cold) region in the center of the image corresponds to the position of A3667. Other cold structures in the map most likely correspond to fluctuations due to receiver noise, primary CMB anisotropies, or artifacts of the offset removal. It is unlikely, given the sensitivity and spatial resolution, that any of the cold spots in the map correspond to serendipitous cluster detections. Over the inner region of the smoothed image, *i.e.* the region not used for offset subtraction, the standard deviation per  $113'' \times 113''$  pixel was found to be  $\simeq 60\mu \text{ K}$ . When deriving this random noise estimate, we assumed that the noise was Gaussian and that each scan was independent. We tested the latter assumption by re-calculating the noise after averaging into groups of first five and then twenty consecutive scans. Grouping the scans in this way before calculating the standard deviation in each pixel did not change the noise estimate. This supports our assumption that the noise was uncorrelated in time; if it had been, this test would have resulted in an increase in the measured standard deviation.

In Figure B2 we compare the inner  $1^\circ \times 1^\circ$  of the Corona map with X-ray and radio images of the same region. Note that for these comparisons, the Corona data were rebinned to the PSPC pixel scale ( $15'' \times 15''$ ) and that this smooths out the ( $113'' \times 113''$ ) pixelization apparent in Figure B1. The white contours in the Figure correspond to the 0.4-2.0 keV X-ray count rate as measured by the PSPC instrument on the ROSAT satellite. The X-ray count rate map was generated from data in the ROSAT public archive using the data reduction pipeline designed for the SHARC Survey (Romer et al. 2000). This data reduction pipeline was based on the ESAS routines of Snowden et al. (1994) and includes the production of a complementary 0.4-2.0 keV exposure map that was used during the model fit-

ting described below (Section 3.3). The black contours correspond to the interferometric radio map at 843 MHz created with the MOST interferometer (Hunstead et al. 1999; Richard Hunstead, private communication).

From Figure B2, it is clear that there is a significant extended cold area close to the center of the X-ray emission. At the centroid ( $20^{\text{h}}12^{\text{m}}28.9^{\text{s}}$ ,  $-56^{\circ}49'51''$  J2000) of the X-ray emission, the temperature decrement in the smoothed Corona map is  $\Delta T_{\text{CMB}} = -154\mu\text{K}$ . There is also some evidence for correlations between hot regions in the image and the MOST radio contours. Taken together, the various correlations between the Corona map and the X-ray and radio maps support the claim in Peterson et al. (2000) that the Corona pointing reconstruction is accurate to within  $\pm 4'$ . The extended radio emission to the north-west of the cluster has been discussed in Röttgering et al. (1997) and Roettiger, Burns and Stone (1999). Both groups suggest that a merging event has produced turbulence in the outer region of the cluster which in turn amplifies magnetic fields, reaccelerates relativistic particles and thus produces radio emission. Radio contamination can be a serious concern when creating SZE images, *e.g.* RX J1347-1145 (Pointecouteau et al. 1999, 2001; Komatsu et al. 2001). However, as there is no evidence of radio contamination in the region of the cluster used for the  $H_0$  measurement (Section 3), *i.e.* the core of the cluster, we do not discuss the radio emission from A3667 again in this paper.

As mentioned above, the random noise per pixel in Figure B1 is  $\simeq 60\mu\text{K}$ . In addition, the images are contaminated by primary CMB anisotropies. We have estimated the level of the CMB contamination in the Corona images to be  $\simeq 38\mu\text{K}$  RMS using the Netterfield et al. (2001) anisotropy power spectrum and assuming a top hat window function with  $10 < l < 400$ . Therefore, some of the features visible in this Figure could correspond to  $> 2\sigma$  CMB fluctuations. For this reason, we cannot rule out that the signal at the position of A3667 is free from CMB contamination. The northern extension of the central cold region could be due to such contamination. Recent observations of A3667 by the multi-frequency Arcminute Cosmology Bolometer Array Receiver (ACBAR, Runyan et al. 2002) on Viper should allow us to quantify the level of CMB contamination in the Corona map because ACBAR has detectors sensitive to frequencies above and below the null<sup>2</sup> in the thermal SZE spectrum.

### 3. DERIVATION OF THE HUBBLE CONSTANT

It has been known for some time (*e.g.* Silk & White 1978; Cavaliere, Danese & Zotti 1979) that a measurement of the thermal SZE toward a cluster could result in a measurement of the Hubble Constant ( $H_0$ ) when it is combined with X-ray observations. This is because the SZE is proportional to the line of sight integral of  $T_e n_e$ , whereas the X-ray surface brightness is proportional to the line of sight integral of  $T_e^{\frac{1}{2}} n_e^2$ . These differing dependencies on the electron temperature and number density, allow one to solve for  $H_0$ , assuming we can find an accurate model for the distribution of these parameters along the line of sight.

<sup>2</sup>The thermal SZE results in a temperature decrement (increment) below (above)  $\nu = 220$  GHz. At the cross over, or null, frequency there is no net change in CMB brightness temperature.

We have used the A3667 data described above to constrain  $H_0$ . We have performed a joint maximum likelihood (Section 3.3) analysis of the Corona and ROSAT PSPC images. During this analysis we have generated many thousands of pairs of simulated ROSAT and Corona A3667 images by making various assumptions concerning both the three dimensional distribution of electrons in the cluster and the performance and noise characteristics of the ROSAT PSPC and Viper Corona instruments (§ 3.1 and 3.2). The technique follows that used by other authors *e.g.* Reese et al. (2002) and Grainge et al. (2002), but is the first application of the method to real space, rather than Fourier space, analysis.

The assumption underlying our analysis was that the number density of electrons in A3667 follows an isothermal  $\beta$ , or King (King 1962), model. The  $\beta$ -model can be parameterized by:

$$n_e = n_{e0} \left( 1 + \left( \frac{r}{r_c} \right)^2 \right)^{-3\beta/2}, \quad (1)$$

where  $n_{e0}$  is the central electron number density;  $r$  is the radius from the center of the cluster; and  $r_c$  is the core radius (Cavaliere & Fusco-Femiano 1978). The X-ray emission from A3667 is clearly not spherically symmetric (Figure B2), so we have further assumed that the cluster has a tri-axial ellipsoidal geometry (Zaroubi et al. 2001 have shown that the ellipsoidal  $\beta$  model provides a good approximation to the three dimensional structure of simulated clusters). We define the radius in Equation 1 as follows:

$$r^2 = x^2 + (\varepsilon y)^2 + (\varepsilon^\zeta l)^2, \quad (2)$$

where the  $x$ ,  $y$ , and  $l$  directions are measured along the principle axes of the ellipsoid. The axes are defined so that  $x$  and  $y$  are in the plane of the sky and  $l$  lies along the line of sight. There are two isomorphic sets of models, those with  $\varepsilon < 1$  and those with  $\varepsilon > 1$ . For the model fitting described below (Section 3.3), we used  $\varepsilon < 1$ , *i.e.* the ellipticity was given by the ratio of the minor to major axes. With this convention, the  $x$  axis lies along the minor axis and the  $y$  axis along the major axis. We have parameterized the stretch along the  $l$  axis by  $\varepsilon^\zeta$ . If  $\zeta = 0$ , then  $\varepsilon^\zeta = 1$ , and the stretch along the  $l$  axis is equal to that along the  $x$  and the ellipsoid is described as prolate. If  $\zeta = 1$ , then  $\varepsilon^\zeta = \varepsilon$ , and the stretch along the  $l$  axis is equal to that along the  $y$  axis and the ellipsoid is described as oblate.

We have chosen to use the ellipsoidal  $\beta$  model with  $\zeta = 0.5$  for our analysis because, as shown by Grainger (2001), this particular model does not result in a significant bias in the measured  $H_0$  value when applied to an ensemble of clusters taken from N-body simulations. The  $\beta$  model is physically motivated; it provides a reasonable, although not exact (see Sarazin 1988), description of the radial dependence of the electron density in isolated spheres of isothermal gas in hydrostatic equilibrium. However, it does have several inadequacies. For example it predicts there will be a finite electron number density even at very large radii from the cluster center. It also includes an

assumption of isothermality when certain clusters, including A3667, are clearly not isothermal (Vikhlinin, Markevitch & Murray 2001a). Moreover, many clusters, including A3667, deviate from spatial symmetry. For these reasons, future analyzes of SZE images would benefit from the use of non-parametric MDM-N-body simulations that have been constrained by observations rather than generic  $\beta$  models.

### 3.1. Simulated ROSAT PSPC Images

For a cluster, the X-ray surface brightness is proportional to the line of sight integral of the square of the electron number density. Assuming  $n_e$  follows Equation 1, using infinite integration limits, and expressing surface brightness as a count rate,  $C_X$ , one obtains;

$$C_X(\theta_r) = C_{X0} \left( 1 + \frac{\theta_r^2}{\theta_c^2} \right)^{-3\beta+1/2}, \quad (3)$$

where  $C_{X0}$  is the central surface brightness and  $\theta_c$  and  $\theta_r$  are related to  $r_c$  in Equation 1 and to  $r$  in Equation 2, respectively, as follows:  $\theta_c = r_c/D_A$  and  $\theta_r = r_{l=0}/D_A$ , where  $D_A$  is the angular diameter distance and  $r_{l=0}$  is given by Equation 2 when  $l = 0$ .

Using Equations 2 and 3, we were able to construct simulated ROSAT PSPC count rate maps of A3667. The simulated PSPC maps were generated in the same energy band (0.4-2.0 keV), with the same pixel size ( $15'' \times 15''$ ) and with the same aim point ( $20^h 12^m 31.20^s$ ,  $-56^\circ 49' 12.0''$ ) as the real observation (Section 2). However, rather than covering the full  $512 \times 512$  pixel area of the ESAS map, the simulated map covered only  $256 \times 256$  pixels (roughly  $1^\circ \times 1^\circ$ ). The eight inputs to the ROSAT PSPC simulation were as follows;

- $\beta$ ,  $\theta_c$  and  $\varepsilon$  to define the shape of ellipsoidal  $\beta$ -model;
- $\phi$  to define the projected inclination angle of cluster. This was defined so that  $\phi = 0^\circ$  when the major axis points toward the West and  $\phi = 90^\circ$  when the major axis points toward the North;
- $\alpha_0$  and  $\delta_0$  to define the sky coordinate of the center of the simulated cluster. These parameters were free to vary and so the center of the simulated map did not necessary coincide with the geometric center of the map;
- $C_{X0}$  to define the 0.4-2.0 keV ROSAT PSPC count rate in a  $15'' \times 15''$  pixel located at  $(\alpha_0, \delta_0)$ . We note that this is the central count rate *before* the correction for the instrument point spread function (PSF) had been applied (see below);
- $C_b$  to define a constant X-ray background in the same units as  $C_{X0}$ .

Before embarking on a maximum likelihood analysis, the simulated images had to be corrected for the effects of the PSPC PSF. This correction was complicated by the fact that the PSF is a function of the radial distance from the center of the field of view. To account for the changing PSF, we convolved each simulated image with 10 different smoothing kernels. Each kernel corresponded to a

model PSF appropriate to a different, evenly spaced, radius from the aim point. The ten resulting convolved images were then co-added using the weighting scheme outlined in Equation B6. This method resulted in a dramatic computational speed-up, compared to a direct calculation of a convolution with a smoothly varying PSF model, because it allowed us to use Fast Fourier Transforms (see Appendix B for more information). Even so, it would have been computationally intensive to convolve the entire  $256 \times 256$  area of the simulated maps, so instead, we convolved only those pixels with a simulated count rate of least 2% of  $C_{X0}$ . The number of pixels meeting that criterion varied depending on the values of the input parameters, but typically only comprised those within a  $\simeq 60$  pixel radius of the center. This simplification was justified by the fact that cluster profiles vary slowly at large radii, meaning the shape of the PSF has little impact on the per pixel count rate outside the cluster core. We numerically tested how much impact PSF convolution has on the outer regions of the cluster model and found it to be insignificant. To create a final simulated image, the center of the original  $256 \times 256$  pixel simulation was replaced by the circular convolved region. We note that the edges of the convolved region were cropped before insertion into the larger map in order to correct for the effects of the artificial periodic boundary condition imposed by the FFT.

### 3.2. Simulated Corona Images

For every simulated ROSAT PSPC X-ray count rate image, we generate a complementary simulated Corona brightness temperature image. In the non-relativistic and low frequency limit, the thermal SZE brightness temperature can be calculated for a given line of sight using the following equation;

$$\frac{\Delta T}{T_{\text{CMB}}} = Y(x \coth(x/2) - 4), \quad (4)$$

where  $T_{\text{CMB}}$  is the average temperature of the CMB (2.73K, Fixen *et al.* 1996);  $x$  is a dimensionless observing frequency,  $x = \frac{h\nu}{kT_{\text{CMB}}}$ ; and the Compton- $Y$  parameter, is given by the line of sight integral

$$Y = \sigma_T \int_{-\infty}^{\infty} \frac{kT_e}{m_e c^2} n_e dl, \quad (5)$$

where  $\sigma_T$  is the Thompson cross section and  $n_e$ ,  $T_e$  and  $m_e$  are the electron number density, temperature and mass respectively.

Each simulated Corona image was generated with the same pixel size ( $113'' \times 113''$ ) and assuming the same observing frequency ( $\nu = 40\text{GHz}$ ) as the raster scan image described above (Section 2). The same input values for  $\beta$ ,  $\theta_c$ ,  $\varepsilon$ ,  $\alpha_0$ ,  $\delta_0$  and  $\phi$  were used to generate both the Corona simulation and the companion ROSAT simulation. In addition, input values for the electron temperature,  $T_e$ , and the central electron number density,  $n_{e0}$ , were required. The electron temperature enters the brightness temperature calculations via the the Compton- $Y$  parameter (Equation 5) and was assumed to be constant throughout the cluster. The central electron number density enters via the normalization of the  $\beta$ -model (Equation 1) and was calculated using the expression given in Equation 7, see section 3.2.1.

The brightness temperature,  $\Delta T$ , is proportional to the line of sight integral of the electron number density (Equations 4 & 5). If  $n_e$  follows a  $\beta$ -model (Equation 1), one can obtain a simple expression for  $\Delta T$  using infinite integration limits that is similar to the one (Equation 3) we used to produce the simulated ROSAT maps, *i.e.*;

$$\Delta T = \Delta T_0 \left(1 + \frac{\theta_r^2}{\theta_c^2}\right)^{-3\beta+1/2}, \quad (6)$$

where  $\Delta T_0$  is the central brightness temperature and  $\theta_r$ ,  $\theta_c$  and  $D_A$  are as defined for Equation 3. Unfortunately, as shown by Puy et al. (2000), using infinite integration limits leads to a significant error in the derived value of  $H_0$ . Therefore, rather than use Equation 6, we integrated Equation 1 numerically over the range  $-14r_c < r < +14r_c$ . By using these limits we avoided included spurious SZE signal at large radii. We note that as a result of our definition of  $r$  (Equation 2), these integration limits defined an iso-density ellipsoid around the cluster.

After the completion of the numerical integrations, the final steps needed to produce a simulated Corona were to convolve the simulated map with the Viper beam and then apply the same offset subtraction scheme used on the real data (Section 2). We performed the latter step because offset subtraction removes certain linear modes from the measured SZE signal and these modes must also be removed from the simulated images before the maximum likelihood analysis takes place.

### 3.2.1. Calculating the Central Electron Number Density

In Appendix A, we outline the derivation of the following expression for the central electron number density;

$$n_{e0} = \sqrt{C_{X0}F} \sqrt{\frac{4\pi(1+z)^4 \varepsilon \zeta \kappa 10^{14}}{D_A \theta_c \Omega} \frac{\Gamma(3\beta)}{\sqrt{\pi} \Gamma(3\beta - 1/2)}}. \quad (7)$$

This expression had to be evaluated before each simulated Corona map was created. The majority of the parameters in the expression have been introduced earlier, but others;  $\kappa$ ,  $\Omega$ ,  $F$ ,  $\zeta$  and  $D_A$ , require additional explanation:

- $\kappa$  is the ratio of electrons to protons in the intra-cluster medium. For our analysis, we used  $\kappa = 1.16$ , which is appropriate for a fully ionized plasma with 30% solar abundances (Feldman 1992).
- $\Omega$  is the area over which the central X-ray count rate,  $C_{X0}$ , is measured (or simulated). For our analysis we used a square ROSAT PSPC pixel ( $15'' \times 15''$ );
- $F$  is a scaling factor that converts an X-ray count rate into an energy flux. The former can be measured with the ROSAT PSPC and the latter can be calculated using theoretical emission models. The value of  $F$  varies with electron temperature ( $T_e$ ), redshift ( $z$ ), metal abundance ( $Z$ ) and hydrogen column density ( $n_H$ ). Assuming isothermality, each cluster has a characteristic  $F$  value, which can be calculated using an X-ray spectral package such as XSPEC (Arnaud 1996). For our analysis of A3667 (Section 3.3), we allowed  $T_e$  and  $n_H$  to vary, but kept the redshift and metal abundance fixed at  $z = 0.055$  and

$Z = 0.3Z_\odot$  respectively: the redshift of the A3667 is well known (more than 100 constituent galaxy redshifts have been measured, Katgert et al. 1998) and the ROSAT count rate varies little with metal abundance (see Hughes & Birkinshaw 1998 for a discussion of how little effect  $Z$  has on measured values of  $H_0$ ). We created a look up table of  $F$  factors covering a range of  $T_e$  and  $n_H$  values using the `raymond` (Raymond & Smith 1976), `wabs` (Morrison & McCammon 1983) and `fakeit` commands in XSPEC, together with the appropriate ROSAT PSPC response function.

- $\zeta$  is the power to which we raise  $\varepsilon$  to obtain the stretch of the beta model in the direction of the line of sight axis (Equation 2). It is impossible to constrain both  $\zeta$  and  $H_0$  from the projected X-ray and SZE data alone. Following, Grainger (2001) we set  $\zeta$  to one half, which implies that the stretch along the line of sight is the geometric mean of the stretch along the other two axes.
- $D_A$  is inversely proportion to the Hubble constant and is also a function of acceleration parameter,  $q_0$ . During our analysis,  $H_0$  was free to vary, but  $q_0$  was fixed at  $q_0 = 0.5$ . We note that at the redshift of A3667, the choice of  $q_0$  has negligible impact on our  $H_0$  determination. This is in contrast to higher redshift SZE observations; Hughes & Birkinshaw (1998) claim that by  $z = 0.5$ , current uncertainties in the underlying cosmological model result in a 10-20% systematic error in  $H_0$ .

In summary, under the assumption that the electron number density follows a  $\beta$  profile, the central density,  $n_{e0}$ , can be expressed as a function of the following parameters;  $C_{X0}$ ,  $\theta_c$ ,  $\beta$ ,  $\varepsilon$ ,  $\zeta$ ,  $\kappa$ ,  $z$ ,  $D_A$  (hence  $H_0$  and  $q_0$ ) and  $F$  (hence  $n_H$ ,  $z$ ,  $Z$  and  $T_e$ ). Of these,  $z$ ,  $Z$ ,  $\kappa$ ,  $q_0$  and  $\zeta$  were fixed during the model fitting.

### 3.3. Calculating the Joint Likelihood of the Simulated Maps

After converting the simulated and observed count rate maps into units of counts per pixel using the ESAS exposure map (Section 2), we calculated the log likelihood of the simulated ROSAT PSPC images using the following expression, under the assumption of Poisson statistics

$$\ln \mathcal{L}_{\text{PSPC}} = \sum_i -\ln(N_{\text{obs}}(i)!) + N_{\text{obs}}(i) \ln(N_{\text{sim}}(i)) - N_{\text{sim}}(i), \quad (8)$$

where  $N_{\text{sim}}(i)$  is number of counts in the  $i^{\text{th}}$  pixel of the simulated map and  $N_{\text{obs}}(i)$  is the corresponding number of observed counts. We carried out the summation over almost all pixels within a  $1 \times 1^\circ$  square centered on the PSPC aim point. The pixels we excluded from the sum had been flagged as belonging to foreground or background X-ray point sources (see Appendix B).

We also calculated the log likelihood function for the simulated Corona images assuming Gaussian noise using the following expression

$$\ln \mathcal{L}_{\text{Corona}} = -\frac{1}{2}(\ln(2\pi|\bar{\Sigma}|) + \Delta' \bar{\Sigma}^{-1} \Delta) \quad (9)$$

where the vector,  $\Delta$ , is defined as  $\Delta = d_{\text{obs}} - d_{\text{sim}}$ ;  $d_{\text{obs}}$  is a vector containing the measured brightness temperature values ( $\Delta T_{\text{obs}}$ ) in each of the pixels under test and  $d_{\text{sim}}$  is the corresponding vector of  $\Delta T_{\text{sim}}$ . In Equation 9,  $\bar{\Sigma}$  is the covariance matrix that describes the correlation between the pixels under test. If the pixels were uncorrelated, then the covariance matrix would be populated by zeros except along the diagonal, where it would be populated by the variance in the corresponding pixel. In the case of the Corona map, the covariance matrix is more complex because the pixels are correlated via atmospheric noise, the finite response time of the detector and the linear interpolation used during the map making process. To evaluate  $\bar{\Sigma}$  we chose 28 pixels lying within one beam (15.7' FWHM) of the center of the co-added, but unsmoothed, Corona map of A3667. We note that we decided to analyze data from this region, rather than the from the whole Corona map, because only near the center of the cluster did the SZE signal exceed the background (statistical plus CMB) noise. Also we wished to avoid regions overlapping with known radio sources. From the 1,518 individual raster images described above (Section 2), we compiled a 28 by 1,518 matrix ( $D$ ) with a column for each of the chosen pixels and a row containing the corresponding brightness temperature measurement. Assuming that for any given pixel, the 1,518 measurements were normally distributed, the covariance matrix for each row of  $D$  was estimated as follows;  $\Sigma = D^T C D$ , where  $D^T$  is the transpose of  $D$  and  $C$  is the centering matrix. The latter is given by  $C = \mathbf{I} - \frac{1}{n}(\mathbf{1}_n \mathbf{1}_n^T)$ . Here,  $\mathbf{I}$  is the identity matrix;  $\mathbf{1}_n$  is a column vector of ones of length  $n$  (in this case  $n = 1518$ ); and  $\mathbf{1}_n^T$  is the transpose of  $\mathbf{1}_n$ . Since the 1,518 scans are independent and the errors are normally distributed, we can determine the covariance matrix for vector  $d_{\text{obs}}$ ,  $\bar{\Sigma}$ , by dividing the covariance matrix for each row of  $D$  by the number of scans; *i.e.*  $\bar{\Sigma} = \Sigma/1518$ . We note that the 28 pixels chosen for the analysis represented only a subset of the total number of pixels within the central beam. The pixels were selected in a checker board fashion, to avoid including any highly correlated nearest neighbor pairs in the analysis. The checkerboard selection method ensured that the covariance matrix was non-singular (*i.e.* invertible) without throwing away too much data.

The joint log likelihood of the two simulated maps,  $\ln \mathcal{L}_{\text{joint}}$ , is given by the sum of the individual log likelihoods, *i.e.*

$$\ln \mathcal{L}_{\text{joint}} = \ln \mathcal{L}_{\text{PSPC}} + \ln \mathcal{L}_{\text{Corona}} + \ln \mathcal{L}_{T_e} + \ln \mathcal{L}_{n_H}, \quad (10)$$

where  $\ln \mathcal{L}_{\text{PSPC}}$  and  $\ln \mathcal{L}_{\text{Corona}}$  were defined above and  $\ln \mathcal{L}_{T_e}$  and  $\ln \mathcal{L}_{n_H}$  are the log likelihoods of the electron temperature,  $T_e$ , and hydrogen column density,  $n_H$ , values used to generate the simulated Corona map. The latter parameters were treated differently to the other free parameters in our model because they have been measured by independent experiments. Under the assumption of Gaussian statistics, their log likelihood functions are given by

$$\ln \mathcal{L}_{T_e} = -\ln(\sigma_{T_e} \sqrt{2\pi}) - (T_e^{\text{in}} - T_e^{\text{obs}})^2 / (2\sigma_{T_e}^2), \quad (11)$$

$$\ln \mathcal{L}_{n_H} = -\ln(\sigma_{n_H} \sqrt{2\pi}) - (n_H^{\text{in}} - n_H^{\text{obs}})^2 / (2\sigma_{n_H}^2), \quad (12)$$

where  $T_e^{\text{in}}$  and  $n_H^{\text{in}}$  are the simulation input values and  $T_e^{\text{obs}}$ ,  $n_H^{\text{obs}}$ ,  $\sigma_{T_e}$  and  $\sigma_{n_H}$  are the measured values and their corresponding 1 sigma errors. In our analysis we used  $T_e^{\text{obs}} = 7.31$  keV;  $\sigma_{T_e} = 0.17$  keV (Markevitch, Vikhlinin & Murray 2001) and  $n_H^{\text{obs}} = 4.71 \times 10^{20}$  cm<sup>-2</sup>;  $\sigma_{n_H} = 1 \times 10^{20}$  cm<sup>-2</sup> (Dickey & Lockman 1990).

### 3.3.1. Best fit model and errors on best fit parameters

As described above, we were able to calculate a joint log likelihood for each pair of simulated A3667 maps using Equation 10. The most likely ellipsoidal isothermal  $\beta$ -model for A3667 was that which maximized the joint likelihood. In order to find the most likely model we created several thousand pairs of simulated images, adjusting the 11 free input parameters ( $C_{X0}$ ,  $C_b$ ,  $\theta_c$ ,  $\beta$ ,  $\varepsilon$ ,  $\phi$ ,  $\alpha_0$ ,  $\delta_0$ ,  $H_0$ ,  $T_e$  and  $n_H$ ) slightly each time. The parameter adjustments were governed by the downhill simplex (Nelder and Mead 1965) routine. We note that the first term ( $-\ln(N_{\text{obs}}(i!))$ ) in Equation 8 is independent of the model being tested, and therefore to speed up the calculations, was not evaluated during the  $\ln \mathcal{L}_{\text{joint}}$  maximization. The best fit values for nine of the eleven free parameters in the fit are given in Table 1. The best fit values for the other two parameters,  $n_H$  and  $T_e$ , were identical (to 3 significant figures) to the values determined by independent experiments (see above). The central electron density corresponding to our best fit model (see Equation 7) is  $n_{e0} = 4.05 \times 10^{-3}$  cm<sup>-3</sup>.

After the most likely  $\beta$ -model had been found, we used the likelihood ratio test (LRT) to define errors on the various input parameters in the fit. The application of the LRT to SZE analysis has been described elsewhere (*e.g.* Hughes & Birkinshaw 1998; Reese et al. 2000), but we review the salient points here. The variable  $\mathcal{S} \equiv -2\ln(\mathcal{L})$  has a minimum  $\mathcal{S}_{\text{min}}$  for the best fit model (*i.e.* when  $\mathcal{L}$  is at a maximum). The Cash statistic (Cash 1979) is defined as  $\mathcal{C} = \mathcal{S} - \mathcal{S}_{\text{min}}$  and is, therefore, equal to zero for the parameter set that defines the best fit model and greater than zero for any other set. The 68% confidence region for a particular input parameter can be estimated by finding the range of values that it can hold for which the Cash statistic that is less than unity. When making the Cash statistic calculations, we hold the parameter at a certain value and then carry out a likelihood maximization by varying the other parameters in the model. Several values of the parameter need to be tested before the  $\mathcal{C} < 1$  region can be determined. The traditional approach to the LRT involves measuring  $\mathcal{L}$ , and hence  $\mathcal{C}$ , at evenly spaced grid points in the  $n$ -dimensional parameter space. However, this approach is computationally prohibitive for a model with 11 parameters. We, therefore, devised a new LRT method which was both more efficient and more objective than the traditional method (it is more objective because it requires no a priori knowledge of the parameter error distributions).

Our method proceeded as follows. First we did a rapid search to find values of the parameter under test that yielded Cash statistic values greater than unity after marginalizing over the other 10 free parameters. We initiated this search by fixing the parameter at a point 50%

above its best fit value. We then performed a likelihood maximization over the remaining 10 free parameters. We repeated this for a fixed point 50% below the best fit value. If these  $\pm 50\%$  points did not yield  $\mathcal{C} > 1$ , then we repeatedly doubled the distance between the tested values until they did. In practice, we only had to use this doubling technique for the Hubble Constant (*i.e.* all the other parameters had  $1\sigma$  errors that were less than 50%). After finding two locations where  $\mathcal{C} > 1$ , and knowing the location of the  $\mathcal{C} = 0$  point, we estimated the locations of the  $\mathcal{C} = 1$  points using a third order beta spline fit. The Cash statistic was re-evaluated at the estimated  $\mathcal{C} = 1$  crossing points and the spline fit performed again. The process was repeated two more times. In this way we built up at least nine  $\mathcal{C}$  measurements; *i.e.* one at, four above and four below the best fit value. With at least nine inputs to the spline fit, it was possible to accurately determine of the  $\mathcal{C} = 1$  crossing points. We performed the LRT error analysis for nine of the eleven<sup>3</sup> free parameters in our model fit, see Figure B4 and Table 1. In general the errors were roughly quadratic, as expected for Gaussian errors; however, in the case of  $H_0$ , the error distribution had a broad tail on the positive side. To demonstrate that the Cash Statistic was a smooth function of  $H_0$ , we tested some additional  $H_0$  values there were not selected by the root finding algorithm (represented by the crosses on Figure B4). Our best fit value for the Hubble Constant is  $64_{-30}^{+96}$  km s<sup>-1</sup> Mpc<sup>-1</sup> (68% confidence limits), see below for a discussion. Best fit values for the other parameters can be found in Table 1. For completeness, we list here published core radius and  $\beta$  values derived from previous fits to the ROSAT PSPC observation of A3667:  $\theta = 2.86'$ ,  $\beta = 0.54$  (Mohr, Mathiesen & Evrard 1999);  $\theta_c = 3.54_{-1.1}^{+1.4}'$ ,  $\beta = 0.67_{-0.12}^{+0.19}$  (Neumann & Arnauad (1999; model B);  $\theta = 4.29 \pm 0.96'$ ,  $\beta = 0.589 \pm 0.051$  (Mason & Myers 2000). Despite the fact that the previous fits were made to average surface brightness profiles, rather than to the image directly, the published values are generally consistent with those in Table 1.

The error on our  $H_0$  measurement is primarily due to the statistical instrument noise in the Corona map; we have  $\simeq 40\%$  error on the measurement of the central temperature decrement and  $H_0 \propto \Delta T^2$ . Other sources of random noise are less important because we have access to high quality X-ray data from ROSAT and Chandra. Our best fit  $H_0$  value compares favorably with other recent SZE measurements;  $H_0 = 60_{-4}^{+4}({}_{-18}^{+13})$  km s<sup>-1</sup> Mpc<sup>-1</sup> (Reese et al. 2002; systematic errors appear in parentheses),  $H_0 = 66_{-11}^{+14}({}_{-5}^{+5})$  km s<sup>-1</sup> Mpc<sup>-1</sup> (Mason, Myers & Readhead 2001),  $H_0 = H_0 = 65_{-7}^{+8}$  km s<sup>-1</sup> Mpc<sup>-1</sup> (Jones et al. 2001). Unlike our analysis, these  $H_0$  measurements were based on observations of multiple clusters (18, 7 and 5 clusters respectively). We note that errors of  $\simeq \pm 30\%$  and exceeding  $\pm 50\%$  are quoted in Jones et al. (2001) sample and Mason, Myers & Readhead (2001) respectively on  $H_0$  measurements derived from single clusters, *e.g.*  $H_0 = 67_{-28}^{+62}$  km s<sup>-1</sup> Mpc<sup>-1</sup> for the A2256  $H_0$  measurement in Mason, Myers & Readhead (2001). These values demonstrates that, even though the errors on our  $H_0$  measurement are large, they are not atypical, especially when compared to other single dish experiments.

#### 4. CONCLUSIONS

As the first stage of the Viper Sunyaev-Zel'dovich Survey (VSZS), we have presented a 40 GHz raster scan map of the region surrounding the  $z = 0.055$  cluster A3667. The cluster was observed during the Antarctic winter of 1999 using the Corona instrument (15.7' FWHM beam) on the Viper Telescope at the South Pole. The Corona image of A3667 is one of the first Sunyaev-Zel'dovich effect (SZE) images of a low redshift cluster. Currently, only the Viper telescope and the Cosmic Background Imager interferometer (Udomprasert, Mason & Readhead 2001) are able to make SZE images of low redshift clusters. One of the advantages of low redshift observations of the SZE is that complimentary data at other wavelengths, for example those necessary to make Hubble Constant estimates, are comparatively easy to obtain. The Corona image of A3367 is also one of the first direct (*i.e.* rather than interferometer) SZE images; only two other clusters have published direct SZE images.

We have used the 40GHz map of A3667 in conjunction with a deep ROSAT PSPC (X-ray) image to make a maximum likelihood fit to an isothermal tri-axial ellipsoidal  $\beta$  model. We have determined 68% confidence regions for nine of the eleven free parameters in the model using a modified Likelihood Ratio Test. Our analysis method includes new approaches to point source detection in X-ray images with varying point spread functions and also to error estimation in multi-dimensional parameter space. These innovations will be applied during the analysis of other VSZS clusters, but are also relevant to other SZE experiments. Our measurement of the Hubble Constant,  $H_0 = 64_{-30}^{+96}$  km s<sup>-1</sup> Mpc<sup>-1</sup>, is in good agreement with previous, SZE determined, measurements. The error on this measurement is large, but not atypical for single dish experiments, and is being driven by instrument noise in the Corona map. Other parameters in the fit have been determined to much higher precision (1-3%).

The Corona instrument was retired at the end of 2000 and replaced with the ACBAR instrument (Runyan et al. 2002). ACBAR offers both improved spatial resolution (5' FWHM beam) compared to Corona and simultaneous multi-wavelength (150, 220, 280 GHz) capabilities. Using ACBAR, in combination with data from CTIO, XMM-Newton and Chandra, we have continued the VSZS and are working toward completion of the SZE, X-ray and weak lensing observations of a complete, luminosity limited, sample of  $\simeq 10$  clusters. These observations will improve our  $H_0$  measurement in several ways. First, long duration ACBAR observations produce more sensitive maps than was possible with Corona (see Kuo et al. 2002). Second, we can minimize the contribution of primary CMB anisotropies in our SZE images by combining data at the three ACBAR observing frequencies (Gomez et al. 2002). This feature becomes important when the instrument noise gets down to the level of the CMB noise and it is noteworthy that most other SZE experiments only operate at a single frequency; Diabolo (Pointecouteau 1999, 2001 & 2002), BOLOCAM (Mauskopf et al. 2000b) and SuZIE (Holzapfel 1997 a&b) are exceptions, but these are not optimized to image low redshift clusters. Third, combining

<sup>3</sup>For the other two,  $n_H$  and  $T_e$ , error estimates were available from independent experiments, see section 3.3.

TABLE 1

THE RESULTS OF THE JOINT MAXIMUM LIKELIHOOD FIT WITH 68% CONFIDENCE LIMITS

$\theta_c$	$\beta$	$C_{X0}^1$	$C_b^1$	$\varepsilon$	$\phi$	$\alpha_0$ (J2000)	$\delta_0$	Notes:
$2.9 \pm 0.1'$	$0.7 \pm 0.02$	$33.4 \pm 0.8$	$2.37 \pm 0.02$	$0.614 \pm 0.009$	$40.0 \pm 0.8^\circ$	$20^h 12^m 28.9 \pm 0.1^s$	$-56^\circ 49' 51 \pm 2''$	

1: Count rates in the 0.4-2.0 keV band in units of  $\times 10^{-3}$  counts  $s^{-1}$  arcmin $^{-2}$

observations of several clusters drawn from a statistically complete sample reduces both random errors and systematic errors associated with orientation bias (*e.g.* Grainger 2001). Finally, the improved spatial resolution of ACBAR over Corona, means that we will be able to use independent beams to probe different lines of the sight through each cluster. We only used data from the central beam of the A3667 Corona image for the analysis above, but by using multiple lines of sight we can reduce the error on the overall measurement. Together, these improvements will allow us to measure the Hubble constant with significantly higher precision than was possible with the Corona observation of A3667 presented herein.

**Acknowledgments** We thank Eric Reese, Jack Hughes and Brian Mason for useful advice concerning the X-ray

analysis and Jullian Borril for assistance with the calculation of the CMB noise in the Corona map. We thank the SHARC collaboration for allowing us to use their reduced PSPC map of A3667 and Dick Hunstead and collaborators for supplying the MOST map of A3367. AKR, CMC, JBP and PG acknowledge financial support from the NASA LTSA program for grant NAG5-7926, "The Viper Sunyaev-Zel'dovich Survey". CMC was the recipient of CMU summer research grants for undergraduates during 1998 and 1999. Computer equipment for this project was purchased using a AAS small research grant. Additional computing resources were kindly made available to us by the PICA group (picagroup.org). Finally we thank the ACBAR collaboration of their continued support of low redshift cluster observations with Viper.

## 5. REFERENCES

## REFERENCES

- Abell, G. O. 1958, ApJS, 3, 211  
 Abell, G. O., Corwin, H. G., & Olowin, R. P. 1989, ApJS, 70, 1  
 Aghanim, N., Górski, K. M., & Puget, J.-L. 2001, A&A, 374, 1  
 Arnaud, K. A. 1996, ASP Conf. Ser. 101: Astronomical Data Analysis Software and Systems V, 5, 17  
 Bardelli, S., Zucca, E., Malizia, A., Zamorani, G., Scaramella, R., & Vettolani, G. 1996, A&A, 305, 435  
 Birkinshaw, M. 1999, Phys. Rep., 310, 97  
 Böhringer, H. et al. 2001, A&A, 369, 826  
 Cash, W. 1979, ApJ, 228, 939  
 Cavaliere, A., Danese, L., & de Zotti, G. 1979, A&A, 75, 322  
 Cavaliere, A. & Fusco-Femiano, R. 1978, A&A, 70, 677  
 Coble, K. et al. 1999, ApJ, 519, L5  
 Cooray, A. R. 1999, MNRAS, 307, 841  
 Cooray, A. R. 2000, MNRAS, 313, 783  
 de Bernardis, P. et al. 2000, Nature, 404, 955  
 De Petris, M. et al. 2002, ApJ, 574, L119  
 David, L. P., Forman, W., & Jones, C. 1999, ApJ, 519, 533  
 Damiani, F., Maggio, A., Micela, G., & Sciortino, S. 1997, ApJ, 483, 350  
 Damiani, F., Maggio, A., Micela, G., & Sciortino, S. 1997, ApJ, 483, 370  
 Desert, F. -. et al. 1998, New Astronomy, 3, 655  
 Dickey, J. M. & Lockman, F. J. 1990, ARA&A, 28, 215  
 Feldman, U. 1992, Physica Scripta Volume T, 46, 202  
 Fixsen, D. J., Cheng, E. S., Gales, J. M., Mather, J. C., Shafer, R. A., & Wright, E. L. 1996, ApJ, 473, 576  
 Freedman, W. L. et al. 2001, ApJ, 553, 47  
 Fusco-Femiano, R., Dal Fiume, D., Orlandini, M., Brunetti, G., Feretti, L., & Giovannini, G. 2001, ApJ, 552, L97  
 Gomez, P.L., Romer, A.K., Peterson, J.B., Cantalupo, C.M. Holzzapfel, W.L., Kuo, C.L., Newcomb, M., Ruhl, J., Goldstein, J., Torbet, E., Runyan, M., 2003, Matter and Energy in Clusters of Galaxies, ASP in press.  
 Grainge, K., Jones, M. E., Pooley, G., Saunders, R., Edge, A., Grainger, W. F., & Kneissl, R. : 2002, MNRAS, 333, 318  
 Grainger, W.F., 2002, PhD thesis University of Cambridge.  
 Grego, L., Carlstrom, J. E., Reese, E. D., Holder, G. P., Holzzapfel, W. L., Joy, M. K., Mohr, J. J., & Patel, S. 2001, ApJ, 552, 2  
 Hanany, S. et al. 2000, ApJ, 545, L5  
 Hasinger, G., Turner, T.J., George, I.M., & Boese, G., 1993, *Legacy*, 3, 46.  
 Holder, G., Haiman, Z. :, & Mohr, J. J. 2001, ApJ, 560, L111  
 Holzzapfel, W. L. et al. 1997a, ApJ, 480, 449  
 Holzzapfel, W. L., Ade, P. A. R., Church, S. E., Mauskopf, P. D., Rephaeli, Y., Wilbanks, T. M., & Lange, A. E. 1997b, ApJ, 481, 35  
 Hughes, J. P. & Birkinshaw, M. 1998, ApJ, 501, 1  
 Joffe, M. et al. 2000, ApJ, 534, L131  
 Jones, M.E, Edge, A.C., Grainge, K., Grainger, W.F., Kneissl, R., Pooley, G.C., Saunders, R., Miyoshi, S.J., Tsuruta, T., Yamashita, K., Tawara, Y., Furuzawa, A., Harada, A., Hatsukade, I., 2001, submitted to MNRAS  
 Katgert, P., Mazure, A., den Hartog, R., Adami, C., Biviano, A., & Perea, J. 1998, A&AS, 129, 399  
 Komatsu, E. et al. 2001, PASJ, 53, 57  
 Kuo, C. L. et al. 2002, submitted to ApJ.  
 Knopp, G. P., Henry, J. P., & Briel, U. G. 1996, ApJ, 472, 125  
 LaRoque, S.J., Carlstrom, J.E., Reese, E.D., Holder, G.P., Holzzapfel, W.L., Joy, M., Grego, L., submitted to ApJ, astro-ph/0204134.  
 Markevitch, M., Sarazin, C. L., & Vikhlinin, A. 1999, ApJ, 521, 526  
 Mason, B. S. & Myers, S. T. 2000, ApJ, 540, 614  
 Mason, B., 2000, PhD Thesis, U. Penn  
 Mason, B. S., Myers, S. T., & Readhead, A. C. S. 2001, ApJ, 555, L11  
 Mauskopf, P. D. et al. 2000a, ApJ, 538, 505  
 Mauskopf, P. D. & et al. 2000b, ASP Conf. Ser. 217: Imaging at Radio through Submillimeter Wavelengths, 115  
 Mohr, J. J., Mathiesen, B., & Evrard, A. E. 1999, ApJ, 517, 627  
 Morrison, R. & McCammon, D. 1983, ApJ, 270, 119  
 elder, J.A., & Mead, R., 1965, Comput. J., 7, 308.  
 Netterfield, C. B. et al. 2002, ApJ, 571, 604  
 Peterson, J. B. et al. 2000, ApJ, 532, L83  
 Peterson, J. B., Radford, S. J. E., Ade, P. A. R., Chamberlin, R. A., O'Kelly, M. J., Peterson, K. M., & Schartman, E. 2002, PASP in press.  
 Pointecouteau, E., Giard, M., Benoit, A., Désert, F. X., Aghanim, N., Coron, N., Lamarre, J. M., & Delabrouille, J. 1999, ApJ, 519, L115  
 Pointecouteau, E., Giard, M., Benoit, A., Désert, F. X., Bernard, J. P., Coron, N., & Lamarre, J. M. 2001, ApJ, 552, 42  
 Pointecouteau, E., Hattori, M., Neumann, D., Komatsu, E., Matsuo, H., Kuno, N., & Böhringer, H. 2002, A&A, 387, 56  
 Puy, D., Grenacher, L., Jetzer, P., & Signore, M. 2000, A&A, 363, 415  
 Raymond, J. C., Cox, D. P., & Smith, B. W. 1976, ApJ, 204, 290  
 Reese, E. D. et al. 2000, ApJ, 533, 38  
 Reese, E. D., Carlstrom, J. E., Joy, M., Mohr, J. J., Grego, L., & Holzzapfel, W. L. 2002, ApJ Submitted; astro-ph/0205350  
 Roettiger, K., Burns, J. O., & Loken, C. 1996, ApJ, 473, 651  
 Roettiger, K., Stone, J. M., & Mushotzky, R. F. 1997, ApJ, 482, 588  
 Roettiger, K., Burns, J. O., & Stone, J. M. 1999, ApJ, 518, 603  
 Romer, A. K. et al. 2000, ApJS, 126, 209  
 Röttgering, H. J. A., Wieringa, M. H., Hunstead, R. W., & Ekers, R. D. 1997, MNRAS, 290, 577



Runyan, M., P.A.R., Bhatia, R.S., Bock, J.J., Daub, M.D., Goldstein, J., Haynes, C.V., Holzapfel, W.L., Kuo, C.L., Lange, A.E., Leong, J., Lueker, M., Newcomb, M., Peterson, J.B., Ruhl, J., Sirbi, G., Torbet, E., Tucker, C., Turner, A.D., Woolsey, D., 2002, submitted to ApJ.  
 Silk, J. & White, S. D. M. 1978, ApJ, 226, L103  
 Snowden, S. L., McCammon, D., Burrows, D. N., & Mendenhall, J. A. 1994, ApJ, 424, 714  
 Sodre, L. J., Capelato, H. V., Steiner, J. E., Proust, D., & Mazure, A. 1992, MNRAS, 259, 233

Soucail, G., Ota, N., Böhringer, H., Czoske, O., Hattori, M., & Mellier, Y. 2000, A&A, 355, 433  
 Sulkanen, M. E. 1999, ApJ, 522, 59  
 unyaev, R.A. & Zel'dovich, Ya. B., 1972, Comm. Astrophys. Sp. Phys., 4, 173.  
 Vikhlinin, A., Markevitch, M., & Murray, S. S. 2001a, ApJ, 551, 160  
 Vikhlinin, A., Markevitch, M., & Murray, S. S. 2001b, ApJ, 549, L47  
 White, D. A., Jones, C., & Forman, W. 1997, MNRAS, 292, 419  
 Wu, X. & Xue, Y. 2000, ApJ, 542, 578  
 Zaroubi, S., Squires, G., de Gasperis, G., Evrard, A. E., Hoffman, Y., & Silk, J. 2001, ApJ, 561, 600

## APPENDIX

### DERIVATION OF THE EQUATION FOR THE CENTRAL ELECTRON NUMBER DENSITY

We detail below how we arrived at Equation 7. We begin with a definition for the the normalization,  $K$ , of the XSPEC Raymond-Smith model (Arnaud et al. 1996);

$$K = \frac{10^{-14}}{4\pi D_L^2} \int n_e n_p dV. \quad (\text{A1})$$

Here  $n_e$  and  $n_p$  are the electron and proton number densities respectively and  $D_L$  is the luminosity distance to the cluster. If we define  $\kappa$  to be the ratio of electrons to protons substituting  $D_L = (1+z)^2 D_A$ , we can rewrite Equation A1 as follows

$$K = \frac{10^{-14}}{4\pi D_A^2 (1+z)^4 \kappa} \int n_e^2 dV. \quad (\text{A2})$$

Expressing the volume element as  $dV = D_A^3 \Omega d\theta_l$ , we can rewrite Equation A2 in terms of an integral along the line of sight,

$$K = \frac{10^{-14} D_A \Omega}{4\pi (1+z)^4 \kappa} \int n_e^2 d\theta_l, \quad (\text{A3})$$

where  $\Omega$  is a solid angle and where the distance along the line of sight is expressed as an angle ( $\theta_l = l/D_A$ ).

If we assume that the electron number density follows an ellipsoidal  $\beta$ -model, we can write down an expression for  $K_0$ , the Raymond-Smith model normalization at the center of the cluster as follows: at the projected cluster centroid the distance simplifies to  $r = \varepsilon^\zeta l$  (since  $x = y = 0$ , see Equation 2). Thus, along the line of sight intersecting the cluster center, the electron number density is given by

$$n_e = n_{e0} \left( 1 + \left( \frac{\varepsilon^\zeta l}{r_c} \right)^2 \right)^{-3/2\beta}, \quad (\text{A4})$$

which is equivalent to the following if we express  $l$  and  $r_c$  as angles;

$$n_e = n_{e0} \left( 1 + \left( \frac{\varepsilon^\zeta \theta_l}{\theta_c} \right)^2 \right)^{-3/2\beta}. \quad (\text{A5})$$

Combining Equations A3 and A5, yields

$$K_0 = \frac{10^{-14} D_A \Omega}{4\pi (1+z)^4 \kappa} \int \left( n_{e0} \left( 1 + \left( \frac{\varepsilon^\zeta \theta_l}{\theta_c} \right)^2 \right)^{-3/2\beta} \right)^2 d\theta_l, \quad (\text{A6})$$

which can be integrated using the following identity<sup>4</sup> and substitution;

$$\int_{-\infty}^{\infty} (1 + A^2 + B^2)^{-C} dA = \sqrt{\pi} \frac{\Gamma(C - 1/2)}{\Gamma(C)} (1 + B^2)^{-C+1/2} \quad (\text{A7})$$

$$u = \frac{\varepsilon^\zeta \theta_l}{\theta_c} \Rightarrow d\theta_l = \frac{\theta_c}{\varepsilon^\zeta} du, \quad (\text{A8})$$

as follows;

<sup>4</sup>Taken from Mason 2000, Equation C.3

$$K_0 = \frac{10^{-14} D_A \Omega n_{e0}^2 \theta_c}{4\pi(1+z)^4 \kappa \varepsilon^\zeta} \int (1+u^2)^{-3\beta} du \quad (\text{A9})$$

$$K_0 = \frac{10^{-14} D_A \Omega n_{e0}^2 \theta_c}{4\sqrt{\pi}(1+z)^4 \kappa \varepsilon^\zeta} \frac{\Gamma(3\beta - 1/2)}{\Gamma(3\beta)}. \quad (\text{A10})$$

We can determine the scaling between  $K$ , the normalization of the Raymond-Smith model, and a ROSAT PSPC count rate for a particular set of input parameters ( $T_e$ ,  $Z$ ,  $z$  and  $n_H$ ) using XSPEC, see Section 3.2.1. Defining,  $F$ , to be the scaling factor between  $K$  and an observed (or simulated) X-ray count rate ( $C_X$ ) in a pixel of size  $\Omega$  (see section 3.2.1), *i.e.*

$$F = \frac{K}{C_X}, \quad (\text{A11})$$

we finally arrive at Equation 7;

$$n_{e0} = \sqrt{C_{X0} F} \sqrt{\frac{4\pi(1+z)^4 \varepsilon^\zeta \kappa 10^{14}}{D_A \theta_c \Omega} \frac{\Gamma(3\beta)}{\sqrt{\pi} \Gamma(3\beta - 1/2)}}. \quad (\text{A12})$$

### REMOVING POINT SOURCES FROM ROSAT PSPC IMAGES

We have devised a method based on Mexican hat wavelet convolutions to identify point sources in X-ray images with variable point spread functions (PSFs). This method is able to exploit the speed of the fast Fourier transform (FFT) by approximating a smoothly varying PSF with  $n$  discrete smoothing kernels. This requires  $O(np \ln(p))$  operations, where  $p$  is the number of pixels in the image, compared to the  $O(p^2)$  operations required for the exact convolution. As  $n$  approaches  $\sqrt{p}$  the method becomes exact, but, in practice,  $n$  can be much less than  $\sqrt{p}$ . We have used this approximation both to find point sources in the ROSAT PSPC image of A3667, see below, and to create simulated PSPC images, see Section 3.1. Our technique could equally well be applied to any PSPC image and, after small modifications, it could also be used to analyze images from other X-ray detectors. The authors have applied it successfully to ROSAT HRI and XMM images.

The method we use to identify the point sources draws on the theoretical framework set up in Damiani et al. (1997, D97 hereafter) and has two parts: the selection of the optimum wavelets and the identification of sources. A brief summary is as follows. First the optimum Mexican hat wavelets to extract point sources located at a set of  $n$  radial distances from the center of the PSPC FOV are selected. The X-ray image under analysis is then convolved with each of these wavelets. Next, a linear combination of the  $n$  convolution products is generated. The resulting combined map approximates a map that has been generated by convolving the X-ray image with a smoothly varying kernel (where that varying kernel describes the optimum wavelet at every position in the image). We note that the optimum wavelets are scaled so that when they are convolved with an X-ray image the result is in units of point source photon counts (see D97). For the analysis of the PSPC observation of A3667 described above (Section 3.3), we used  $n = 10$  different wavelets corresponding to 10 evenly spaced distances from the center of the PSPC FOV.

The Mexican hat wavelet used as our smoothing kernel is defined by:

$$z(x, y, a) = \frac{\sqrt{x^2 + y^2}}{a} \\ g(x, y, a) \equiv g(z(x, y, a)) = (2 - z^2)e^{-z^2/2}, \quad (\text{B1})$$

where,  $a$  is the so called scale parameter. Using an optimization procedure, we can find the kernel best suited to find point sources at a particular radius, *i.e.* the value of  $a$  that maximizes the following expression:

$$c(a) = \sum_i \sum_j \frac{g(i - i_0, j - j_0, a) s(i, j)}{a}, \quad (\text{B2})$$

where  $s(i, j)$  is the simulated point source image positioned at the center,  $(i_0, j_0)$ , of a large array and  $s$  is normalized so that  $\sum_i \sum_j s(i, j) = 1$ . We carry out this optimization for a set of  $n$  distances,  $r_k$ , from the center of the PSPC FOV. For each of the chosen distances we maximize  $c(a)$  by varying  $a$  using the Nelder-Mead downhill simplex algorithm and solve for  $a_k$ , where  $k \in \{0, 1, \dots, n-1\}$ .

To generate the simulated point source images, we used the empirically determined PSPC PSF model of Hasinger et al. (1993). For any given point source, this model is a function of both its photon energy spectrum and its radial distance. For our analysis, we made the simplifying assumption that all point sources can be described by a generic absorbed AGN spectrum ( $n_H = 4 \times 10^{20} \text{ cm}^{-2}$ ,  $\alpha = -1$ ), since AGN's comprise the majority of the ROSAT point source population (Mittaz et al. 1999).

After determining the optimal wavelet for a set of distances from the center of the PSPC FOV, we scaled the wavelets so that the magnitude of point source shaped objects was preserved in the convolution. The scaled Mexican hat wavelet

that we use is for each of our  $k$  chosen distances is

$$g_k(i, j) = \frac{1}{a_k c(a_k)} g(i, j, a_k). \quad (\text{B3})$$

Next, using FFT's, we convolved the X-ray image under analysis with each of the  $n$  optimum wavelets:

$$\rho_k(i, j) = \sum_l \sum_m g_k(l - i, m - j) v(l, m), \quad (\text{B4})$$

where  $v(i, j)$  describes the X-ray photon count rate image. The convolved maps  $\rho_k$  are then combined together:

$$\hat{\rho}(i, j) = \sum_{k=0}^{n-1} h_k(i, j) \rho_k(i, j) \quad (\text{B5})$$

where the weights  $h_k$  are defined as follows

$$r = \sqrt{(i - i_0)^2 + (j - j_0)^2}$$

$$h_k(i, j) \equiv h_k(r) = \begin{cases} 0 & \text{if } r < r_{k-1} \\ \frac{r - r_{k-1}}{r_k - r_{k-1}} & \text{if } r_{k-1} \leq r \quad \& \quad r < r_k \\ \frac{r_{k+1} - r}{r_{k+1} - r_k} & \text{if } r_k \leq r \quad \& \quad r < r_{k+1} \\ 0 & \text{if } r > r_{k+1} \end{cases} \quad (\text{B6})$$

and  $(i_0, j_0)$  is the center of  $v(i, j)$ . By virtue of the wavelet scaling (equation B3), the units of the combined map are such that if a point source was centered on position  $(i, j)$  then  $\hat{\rho}(i, j)$  would be an estimate of the photon count rate from that point source. This count rate can then be converted into an estimate of the number of photons collected from a point source, by multiplication with an appropriate exposure map ( $E(i, j)$ ). Therefore, to excise point sources from an X-ray image, we can simply apply a photon count threshold to  $\hat{\rho}(i, j) \times E(i, j)$ .

For the A3667 analysis described in section 3.3 we excluded pixels above an 65 count threshold in  $\hat{\rho}(i, j) \times E(i, j)$  from the maximum likelihood analysis. We also excluded pixels within a 4 pixels radius of  $\hat{\rho}(i, j) \times E(i, j) > 65$  count regions. We note that this 80 count threshold was chosen to meet the specific needs of the analysis described in section 3.3. A different type of analysis, a different cluster observation, or a different instrument would likely have led to a different choice.

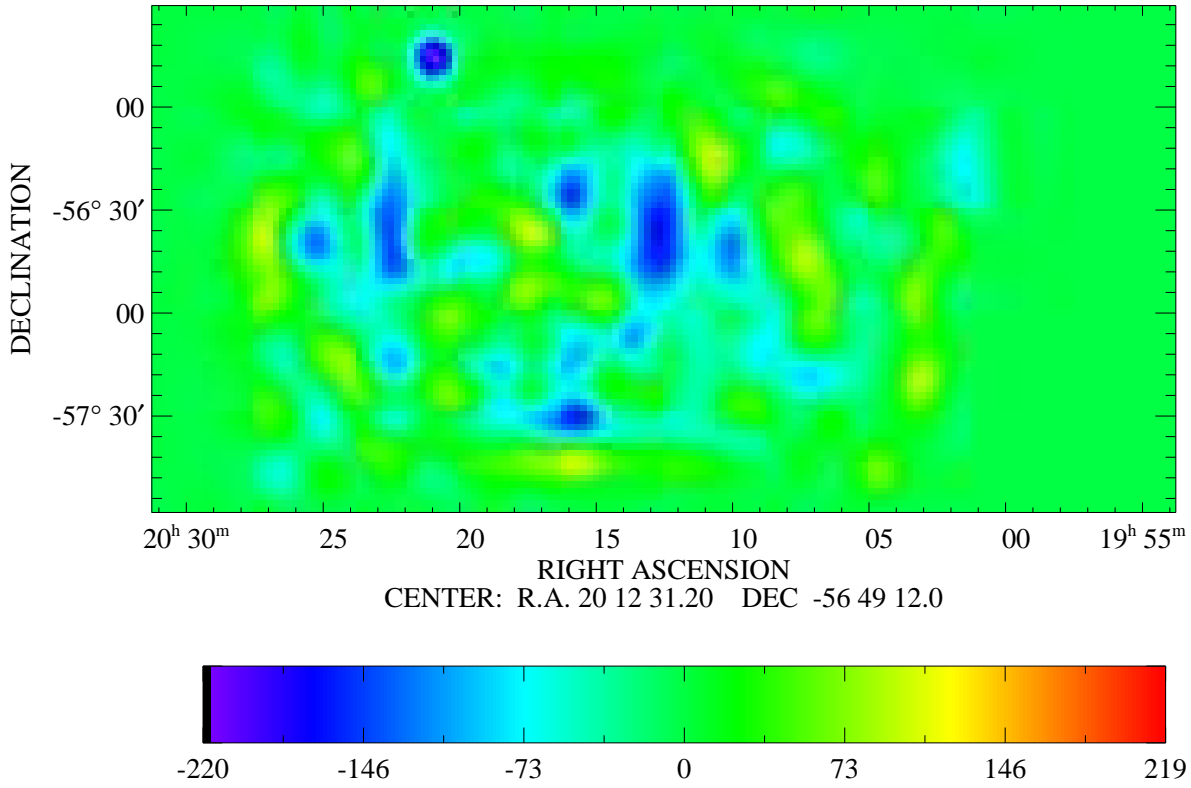


FIG. B1.— The  $3.6^\circ \times 2^\circ$  area of the Corona 40 GHz map of A3667 in units of  $\mu K$ . The map is a result of averaging 1518 raster scans of the region, for a total exposure time of  $\simeq 36$  hours. The map has been smoothed with a  $10.3'$  FWHM Gaussian kernel, which gives it an effective resolution of  $18'$  FWHM (the beam size of the instrument is  $15.7'$ ). The pixel size is  $113'' \times 113''$ . The large ( $\simeq 30'$  in length), cold (blue), area in the center of the map coincides with the X-ray emission from the cluster.

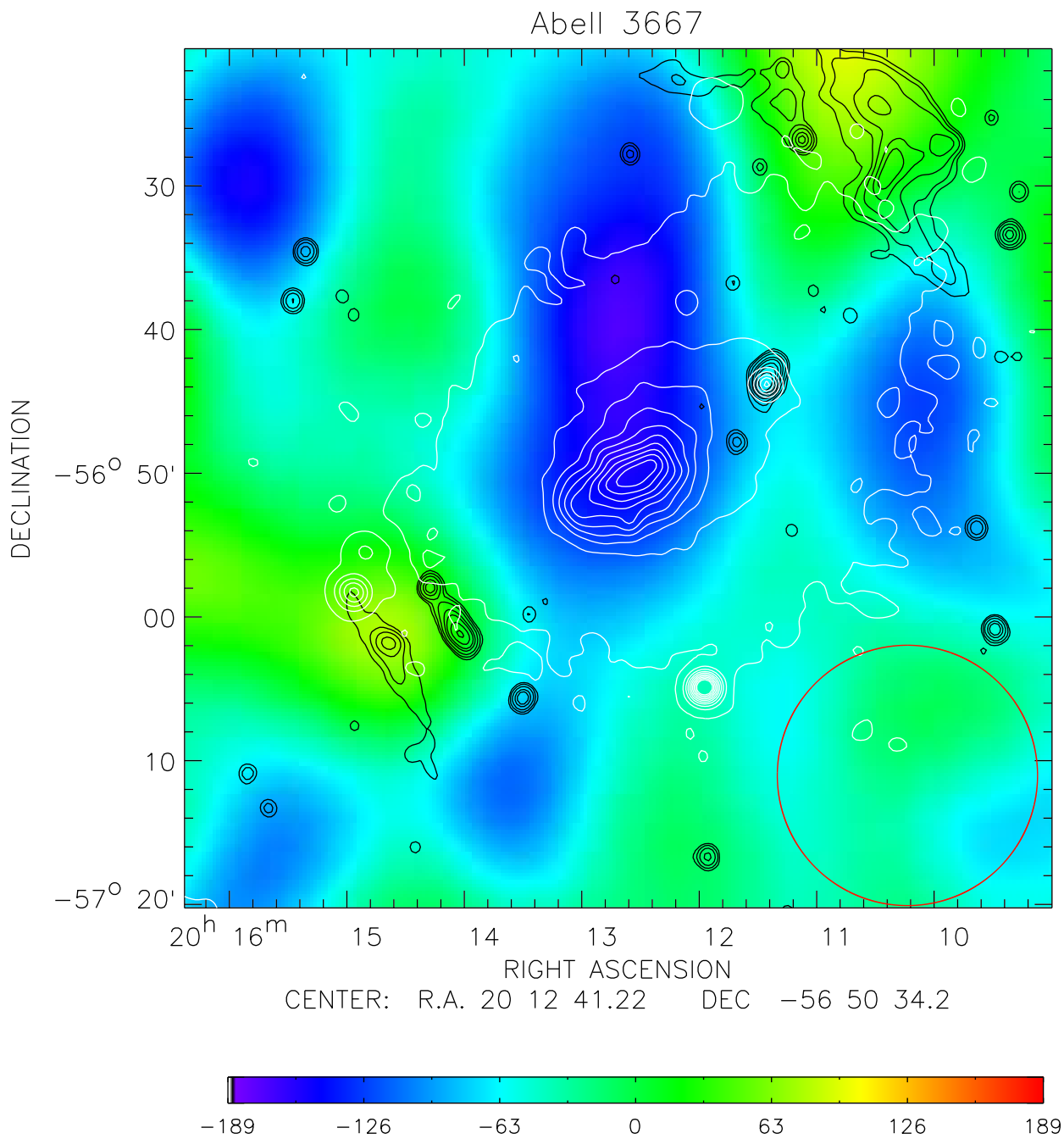


FIG. B2.— The central  $1 \times 1^\circ$  region of the Corona map in units of  $\mu K$ . The Corona have been re-binned to the ROSAT PSPC pixel scale ( $15'' \times 15''$ ). The black contours represent the MOST radio (843 GHz) observation of A3667 (Hunstead, private communication). We note the correspondence between the extended radio halo and hot spots in the Corona map. The white contours represent the ROSAT PSPC 0.4-2.0 keV image of A3667. The diameter of the red circle in the bottom right corner shows the effective beam ( $18'$  FWHM) of the Corona map.

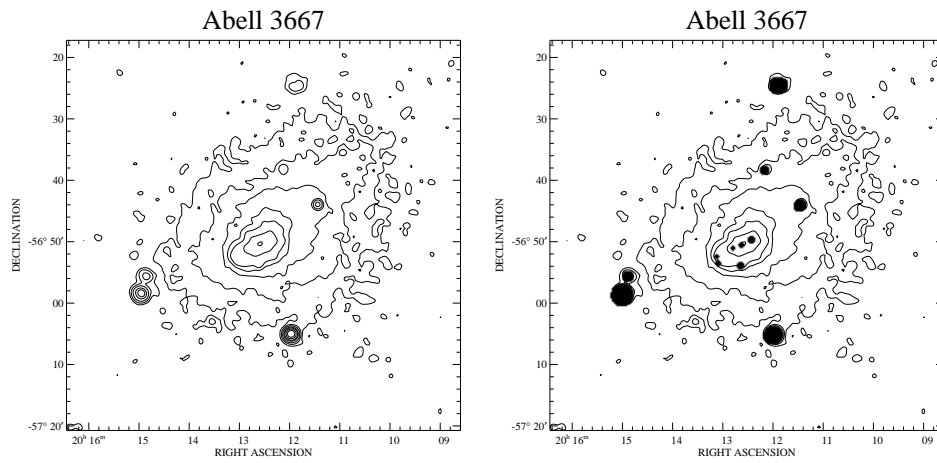


FIG. B3.— The 0.4-2.0 keV PSPC count rate image of A3667 (right) and the same image after (right) point sources have been masked out. The masked regions were not included in the maximum likelihood analysis.

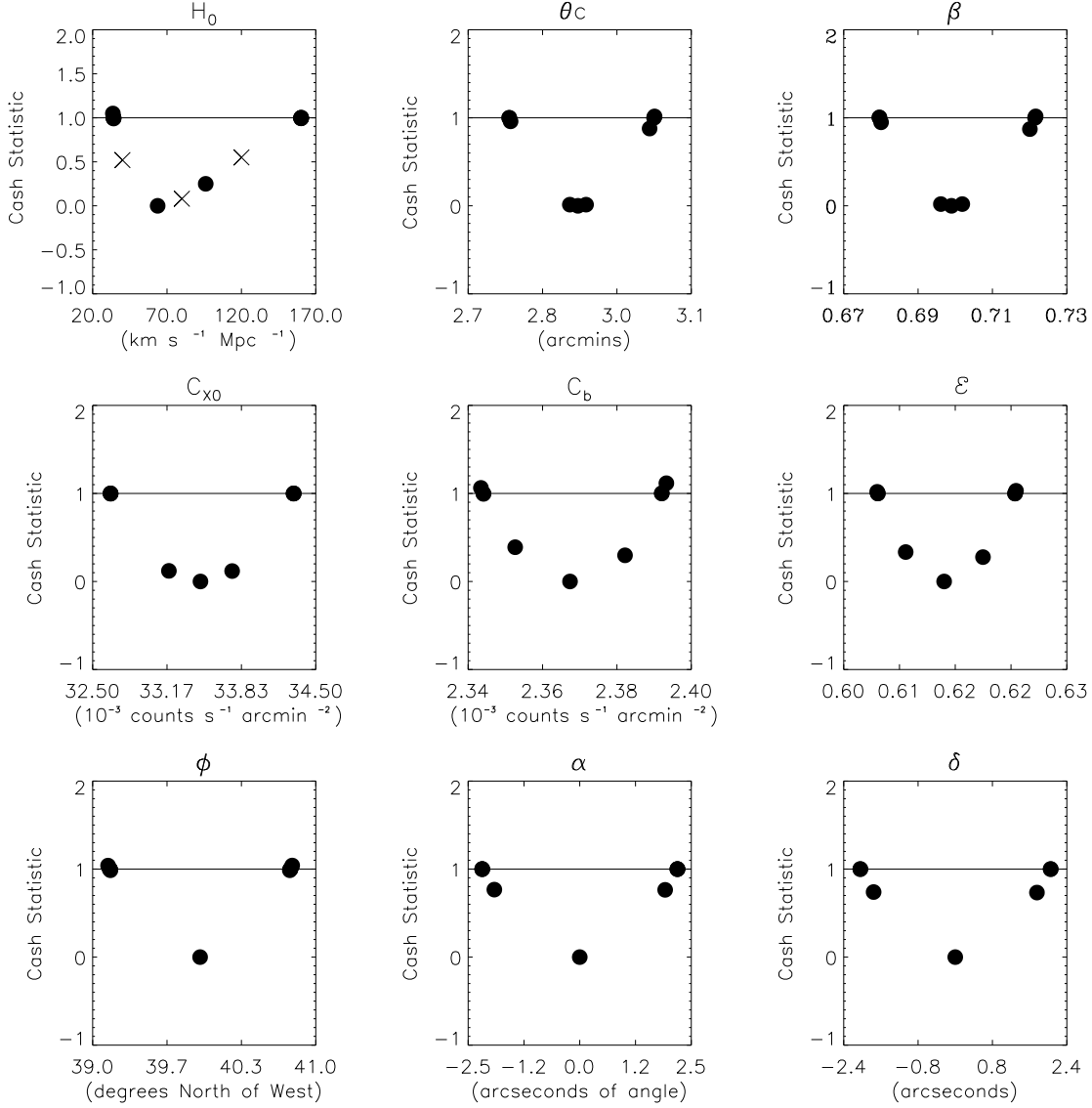


FIG. B4.— The Cash statistic as a function of: Hubble Constant (top left); core radius (top center);  $\beta$  (top left); central (0.5-2.0 keV) count rate (center left); background (0.5-2.0 keV) count rate (center center); ellipticity (center right); orientation angle (bottom left); central right ascension coordinate (bottom center); central declination coordinate (bottom right). The  $C = 1$  crossing points define the edges of the 68% confidence region for each parameter. The black dots indicate the parameter values chosen by our automated error analysis software; notice how few values need to be tested before the  $C = 1$  crossing points were found. For  $H_0$  we added three extra test values by hand to demonstrate that there were not additional minima in the  $C(H_0)$  function.